Short Papers

Analysis of Slot-Coupled Transitions from Microstrip-to-Microstrip and Microstrip-to-Waveguides

Amjad A. Omar and Nihad I. Dib

***Abstract*— This paper provides an accurate, versatile, and computationally efficient method for the analysis of slot-coupled transitions from microstrip-to-microstrip, and microstrip-to-rectangular and parallel-plate waveguides. The accuracy of this method is ensured by satisfying all the boundary conditions through a mixed electric–magnetic current integral equation formulation, combined with the moment method. Computational efficiency is achieved by limiting the discretization to only the strips and apertures and by using the accurate and rapidly convergent complex images. To verify the accuracy of this method, the transitions are analyzed using the finite-difference time-domain (FDTD) method. Experimental results are also obtained for some structures. Close agreement is found between the complex image results, the FDTD results, and experiment over a wide frequency range.**

***Index Terms*— Complex images, integral equation, microstrip, slot, waveguides.**

I. Introduction

There has been a recent trend toward building circuits which have more than one dielectric layer and more than one level of metallization to reduce the size of microwave and millimeter-wave circuits. Some of the metallization layers are used to isolate the active from the passive elements to reduce the parasitic coupling between them. To this end, it is important to study the transition between microstrip and microstrip through a slot in the common ground plane, as shown in Fig. 1.

Two other important classes of transitions are the microstrip-to-parallel-plate waveguide (MS–PWG) and microstrip-to-rectangular waveguide (MS–RW) transitions via a slot in the microstrip ground plane (Figs. 2 and 3) [1], [2]. These transitions are important in high-Q filters, high-Q oscillators, and nonreciprocal components. The ability to analyze these transitions becomes very important, especially in the millimeter-wave frequency range.

To achieve optimum design of the different transitions, it is important that an accurate and computationally efficient method be developed which can be easily interfaced with available optimization design software. As far as is known, there have been little or no publications on the theoretical analysis of slot-coupled microstripline (MS)-to-waveguide transitions [1]. However, several methods have been presented in the literature to analyze the transition between two microstriplines (MS–MS) through a slot, shown in Fig. 1. Some of these methods, like the finite-difference time-domain (FDTD) method and transmission-line matrix (TLM) method, require the discretization of the entire volume of the circuit. They are, therefore, slowly convergent and require excessive memory. Also, the application of the electric-field integral-equation technique (EFIE) requires segmenting the entire conducting surface of the transition, including the infinite microstrip ground plane.[1] Therefore, the EFIE is numerically inefficient for solving the aperture coupling problem.

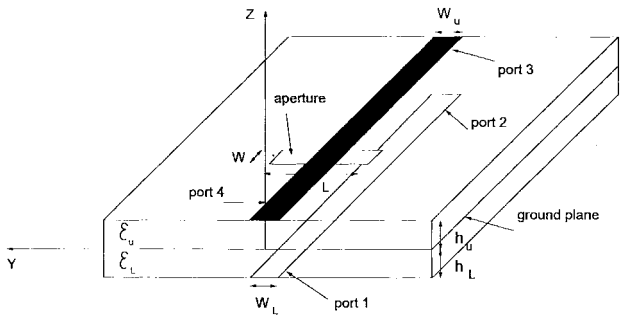

Fig. 1. A three-dimensional (3-D) view of the microstrip-to-microstrip transition via an aperture.

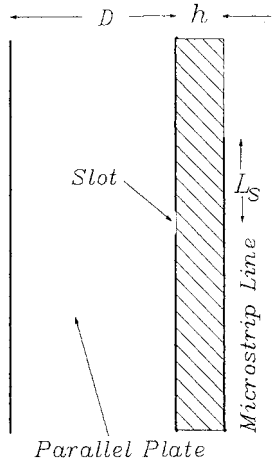

Fig. 2. The MS–PWG transition.

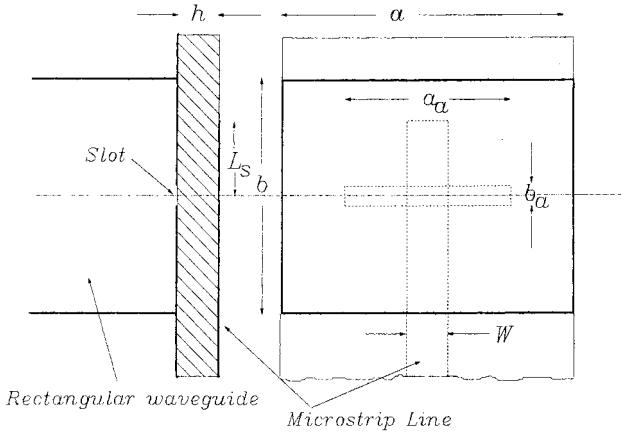

Fig. 3. The MS–RW transition.

Manuscript received February 22, 1996; revised March 24, 1997.

A. Omar is with the Royal Scientific Society, Princess Sumayya University College of Technology, Amman, Jordan.

N. I. Dib is with the Department of Electrical Engineering, Jordan University of Science and Technology, Irbid, Jordan.

Publisher Item Identifier S 0018-9480(97)04465-7.

[1] **em**, Sonnet Software Inc., Liverpool, NY, 13090.

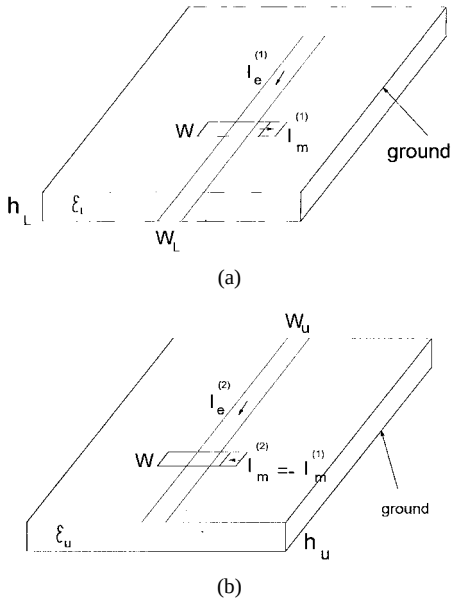

Fig. 4. Splitting the MS–MS transition into two sub-problems equivalent to the upper and lower half spaces, respectively. (a) Lower half space. (b) Upper half space.

A more efficient form of the integral equation technique was applied in [3] for the analysis of the MS–MS transition. Unlike the EFIE, which uses only electric currents, this technique uses both electric and magnetic currents, which flow on the strips and apertures, respectively. This limits the discretization to only the strips and apertures, and, thus, saves a lot of memory and computation time. However, the time-consuming numerical integrations of Sommerfeld integrals are evaluated in [3] to obtain the spatial Green's functions of the structure. Therefore, there is still a need for a technique which is faster and, hence, more suitable for use with CAD programs.

In this paper, a mixed electric–magnetic current integral equation formulation similar to that in [3] is used. However, this paper's Green's functions for the coupling between the electric currents of the MS's, magnetic current of the aperture, and for the cross coupling between the electric and magnetic currents, are all calculated using the accurate and rapidly convergent complex image technique [4], [5]. The only case where complex images are not used is when the Green's functions of the rectangular waveguide (RW) are evaluated. In this case, the real waveguide images are used instead. The complex image technique avoids the time-consuming numerical integration of Sommerfeld integrals and yields at least a ten-fold reduction in computation time with less than 1% error, as compared to the numerical integration. These complex images include the effect of the surface waves and leaky waves and, therefore, have no restriction on the substrate thickness.

To verify the accuracy of the results obtained using the complex image technique, the same transitions are analyzed using the FDTD method. The FDTD formulation is simple and well known [6]–[8] and, thus, will not be presented here. Instead, the emphasis will be on the formulation of the mixed electric–magnetic current integral equation and the use of the computationally fast complex image technique to evaluate all the Green's functions.

II. Theory

A. MS–MS Transition

To solve the MS–MS problem, the structure of Fig. 1 is split into two sub-problems, equivalent to the lower and upper microstrips, as shown in Fig. 4(a) and 4(b), respectively. Equivalent electric and magnetic currents flow on the strips and apertures, respectively, of both sub-problems to satisfy the boundary conditions, as follows.

1) The continuity of the tangential electric field on the aperture is enforced by choosing the magnetic current on the aperture of the lower sub-problem, which flows along the y-direction [$I_{my}^{(1)}$ of Fig. 4(a)], to be equal and opposite to that on the aperture of the upper sub-problem [$I_{my}^{(2)}$ of Fig. 4(b)].
2) The continuity of the tangential magnetic field on the aperture is satisfied by the following equation:

$$H_y^{(1)}\left(I_{ex}^{(1)}\right) + H_y^{(1)}\left(I_{my}^{(1)}\right) = H_y^{(2)}\left(I_{ex}^{(2)}\right) + H_y^{(2)}\left(I_{my}^{(2)}\right) \quad (1)$$

where $I_{ex}^{(1)}$ and $I_{ex}^{(2)}$ are the x-directed electric currents flowing on the lower and upper microstrips, respectively, while $I_{my}^{(1)}$ and $I_{my}^{(2)}$ are the y-directed magnetic currents flowing on the aperture in the lower and upper sub-problems, respectively. $H_y^{(i)}(I_{ex}^{(i)})$ and $H_y^{(i)}(I_{my}^{(i)})$ denote the y-directed magnetic field on the aperture of the ith sub-problem caused by an x-directed electric current on the MS and a y-directed magnetic current on the aperture, respectively.

The fields in (1) can be expressed in terms of the mixed potentials of electric and magnetic currents [9], as follows:

$$H_y^{(i)}\left(I_{my}^{(i)}\right) = -j\omega \int_{\text{Aper.}} G_{F_{yy}}^{(i)}(r/r')J_{my}^{(i)}(r')\,dS' + \frac{1}{j\omega}\int_{\text{Aper.}} \frac{\partial}{\partial y}\left[G_{qm}^{(i)}(r/r')\frac{\partial J_{my}^{(i)}}{\partial y'}\right] dS' \quad (2)$$

$$H_y^{(i)}\left(I_{ex}^{(i)}\right) = H_{y,xx}^{(i)}\left(I_{ex}^{(i)}\right) + H_{y,zx}^{(i)}\left(I_{ex}^{(i)}\right) \quad (3)$$

where

$$H_{y,xx}^{(i)}\left(I_{ex}^{(i)}\right) = \left[\vec{\nabla} \times \int_{M_i} G_{A_{xx}}^{(i)}(r/r')J_{ex}^{(i)}(r')\hat{x}\,dS'\right]\cdot \hat{y} \quad (4)$$

$$H_{y,zx}^{(i)}\left(I_{ex}^{(i)}\right) = \left[\vec{\nabla} \times \int_{M_i} G_{A_{zx}}^{(i)}(r/r')J_{ex}^{(i)}(r')\hat{z}\,dS'\right]\cdot \hat{y}. \quad (5)$$

In (2), use has been made of the continuity equation for magnetic current and charge [9]. In (2), $G_{F_{yy}}^{(i)}$ is the Green's function for the y-directed electric vector potential due to a y-directed magnetic current in the ith sub-problem [10], while $G_{qm}^{(i)}$ is the scalar potential due to a magnetic charge [10]. $G_{A_{xx}}^{(i)}$ in (4) is the Green's function for the x-directed magnetic vector potential due to an x-directed electric current in the ith sub-problem, while $G_{A_{zx}}^{(i)}$ in (5) is the Green's function for the z-directed magnetic vector potential due to an x-directed electric current, with both source and field located inside a microstrip substrate. These Green's functions are given in Appendix A. The area M_i, over which the integrals are performed, is the microstrip of the ith sub-problem.

3) The vanishing of the tangential electric field on the MS's of the upper and lower sub-problems is satisfied by the following equation:

$$E_x^{(i)}\left(I_{ex}^{(i)}\right) + E_x^{(i)}\left(I_{my}^{(i)}\right) = -E_x^{\text{ext}} \quad (6)$$

where $i = 1$ and 2 corresponds to the lower and upper sub-problems, respectively. $E_x^{(i)}$ and E_x^{ext} are the scattered and impressed electric fields, respectively.

The electric and magnetic current densities are expanded as follows:

$$J_{ex}^{(i)}(r') = \sum_{n=1}^{N_e^{(i)}} I_{ex,n}^{(i)} f_n^e(x')\tau_n^e(y') \quad (7)$$

$$J_{my}(r') = \sum_{n=1}^{N_m} I_{my,n} f_n^m(y')\tau_n^m(x') \quad (8)$$

where $N_e^{(i)}$ and N_m are the number of segments on the microstrip of the ith sub-problem and aperture, respectively. f_n^e and f_n^m are pulse basis functions, which are unity along the nth electric or magnetic current segments, respectively, and zero elsewhere. τ_n^e and τ_n^m account for the edge condition on the strips and apertures [11], respectively, and are given by

$$\tau_n^e(y') = \frac{1}{\pi\sqrt{\left(\frac{W_e^{(i)}}{2}\right)^2 - (y')^2}}$$
$$\tau_n^m(x') = \frac{1}{\pi\sqrt{\left(\frac{W_m}{2}\right)^2 - (x')^2}} \tag{9}$$

where $W_e^{(i)}$ and W_m are the widths of the microstrip of the ith sub-problem and the width of the aperture, respectively. The choice of the basis functions in (7) and (8) was first validated by Glisson and Wilton [12], who showed that the use of pulse basis functions instead of rooftop basis functions has very little effect on the moment-method solution. This choice, however, significantly reduces the computations [13].

The Galerkin moment method [14] is then applied to (1) and (6), using the expansion functions of (7) and (8) also as weighting functions. This results are shown in the following matrix equation:

$$\begin{bmatrix} V_{\rm ext}^{(1)} \\ \underline{0} \\ \underline{0} \end{bmatrix} = \begin{bmatrix} [Z_{\rm ee}^{(1)}] & [Z_{em}^{(1)}] & [0] \\ [Z_{me}^{(1)}] & [Z_{\rm mm}^{(1)}] + [Z_{\rm mm}^{(2)}] & -[Z_{me}^{(2)}] \\ [0] & [Z_{em}^{(2)}] & [Z_{\rm ee}^{(2)}] \end{bmatrix} \begin{bmatrix} \underline{I}_{ex}^{(1)} \\ \underline{I}_{my}^{(1)} \\ \underline{I}_{ex}^{(2)} \end{bmatrix} \tag{10}$$

where $Z_{\rm ee}^{(1)}$ and $Z_{\rm ee}^{(2)}$ are the lower and upper microstrip impedance matrixes, respectively [15]. $Z_{\rm mm}^{(1)}$ and $Z_{\rm mm}^{(2)}$ are the lower and upper magnetic–magnetic (aperture) impedance matrixes, respectively. They are the dual of the electric–electric impedance matrixes in [4]. $Z_{me}^{(1)}$ and $Z_{me}^{(2)}$ are the matrixes for the magnetic voltages on the aperture due to unit electric currents on the microstrips of the lower and upper sub-problems, respectively. Since these two matrixes have similar forms, only the expression of $Z_{me}^{(1)}$ is given in Appendix B. $Z_{em}^{(1)}$ and $Z_{em}^{(2)}$ are the matrixes for the electric voltages on the microstrips of the lower and upper sub-problems, respectively, due to unit magnetic currents on the aperture. These matrixes were derived following the same procedure explained in Appendix B for obtaining $Z_{me}^{(1)}$. The details of the calculations of the self terms of the matrixes $Z_{\rm ee}$ and $Z_{\rm mm}$ in (10) can be found in [15].

It is important to mention that the Green's functions in this paper are evaluated using the complex images technique [4], [5], as explained in Appendix A. This technique avoids the numerical integration of Sommerfeld integrals used to perform the inverse Fourier transform of the spectral functions. Instead, the spectral functions are approximated as finite sums of complex exponentials using Prony's method [16] and the Sommerfeld integral is performed analytically using Sommerfeld's identity, resulting in a small number of images with complex amplitudes and complex locations. The authors' numerical tests have revealed that the complex images provide at least a ten-fold reduction in computation time with less than 1% error as compared to the numerical integration of Sommerfeld integrals.

B. MS–PWG and MS–RW Transition

To solve the MS–PWG or MS–RW transitions shown in Figs. 2 and 3, respectively, (10) needs to be slightly modified, as follows:

$$\begin{bmatrix} V_{\rm ext}^{(1)} \\ 0 \end{bmatrix} = \begin{bmatrix} [Z_{\rm ee}^{(1)}] & [Z_{em}^{(1)}] \\ [Z_{me}^{(1)}] & [Z_{\rm mm}^{(1)}] + [Z_{\rm mm}^{(2)}] \end{bmatrix} \begin{bmatrix} \underline{I}_{ex}^{(1)} \\ \underline{I}_{my}^{(1)} \end{bmatrix}. \tag{11}$$

All the matrixes in (11) remain the same as in (10), except for the magnetic–magnetic coupling matrix of the upper sub-problem $[Z_{\rm mm}^{(2)}]$, which results from a different set of Green's functions. In the case of MS–PWG transition, the complex image Green's functions correspond to a magnetic current between two parallel conducting plates. The expressions for these Green's functions can be found in [17]. In the case of MS–RW transition, the Green's functions needed are those for a magnetic current inside a rectangular waveguide. To avoid the complexity of the complex image solution of a waveguide, only the classical real images are used. The computational effort involved is explained in the following section.

III. Numerical Results

A. MS–MS Transition

Fig. 5 compares the S-parameters of the MS–MS transition obtained using the complex image technique, the numerical integration of Sommerfeld integrals in [3], and FDTD. Fig. 5(a) shows that the difference in $|S_{11}|$ between the complex image results and the results of [3] is less than 1 dB over the range of frequencies between 2 and 4 GHz. Fig. 5(b) shows a maximum difference in $|S_{21}|$ of 0.15 dB, while Fig. 5(c) shows a maximum difference in $|S_{31}|$ of 1.2 dB. However, there is practically no difference between the complex image results and the FDTD results.

To demonstrate the accuracy of the complex image technique at higher frequencies, Fig. 6 shows a comparison with experimental results and FDTD theoretical results, over the range of frequencies between 0.5 and 11 GHz for an MS–MS transition. The maximum difference between the complex image results and the experiment is less than 2 dB over the whole frequency range investigated. This difference may be attributed to the fact that the authors' model assumes infinitely thin perfect conductors and infinitely wide ground planes. Fig. 7 shows $|S_{21}|$ and $|S_{31}|$ as compared to FDTD results for the same frequency range and dimensions of Fig. 6. The maximum difference in $|S_{21}|$ and $|S_{31}|$ is less than 2 dB.

The above results verify the accuracy of the complex image method as compared with the FDTD method and experiments. As for computational efficiency, the authors' method requires less than 4 min per frequency point on an 80 386 40 MHz PC. On the other hand, the FDTD code had to be executed on a DEC ALPHA machine and the entire volume of the structure had to be discretized.

B. MS–Parallel Plate and MS–Rectangular Waveguide Transitions

Fig. 8 shows $|S_{11}|$ of an MS–PWG transition computed using both the complex image technique, described above, and the FDTD method. Clearly, the two sets of results agree very well. It should be mentioned that there has been no attempt to optimize the structure to get better coupling.

As for the MS–RW transition, Fig. 9 compares $|S_{11}|$, calculated using the complex image method, with that calculated using the FDTD method. The maximum difference is only 3%. The number of real images used to calculate each of the Green's functions inside a RW is 30×30.

The results for the MS–MS, MS–PWG, and MS–RW transitions clearly show the accuracy as well as the versatility of the complex image solution of the transitions in terms of the ability to solve a variety of transitions. Currently, work is being done to extend this technique to other multilayered transitions (e.g., coplanar waveguide (CPW) patch, CPW–RW).

IV. Conclusion

In this paper, an accurate and computationally efficient method for solving the problems of aperture coupling from microstrip-to-microstrip, microstrip-to-parallel plate, and MS–RW transitions has

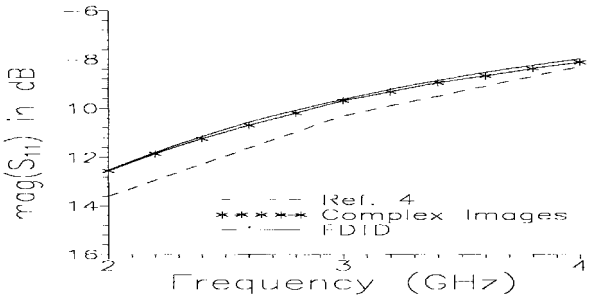

(a)

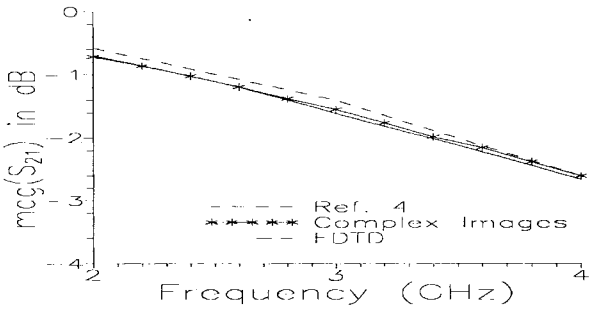

(b)

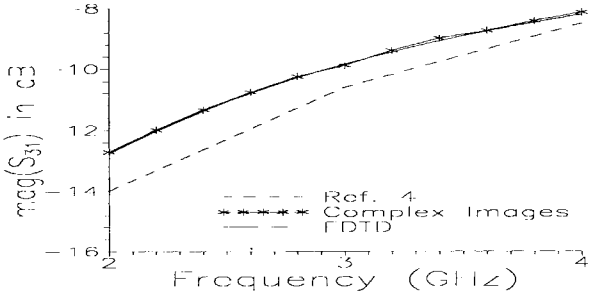

(c)

Fig. 5. Comparison between the authors' results, FDTD results, and the results of [3] for the S-parameters of two aperture coupled microstrips. (a) $|S_{11}|$, (b) $|S_{21}|$, (c) $|S_{31}|$. ($W_u = W_L = 0.254$ cm, $\varepsilon_u = \varepsilon_L = 2.22$, $h_u = h_L = 0.0762$ cm, $L = 1.5$ cm, $W = 0.11$ cm.)

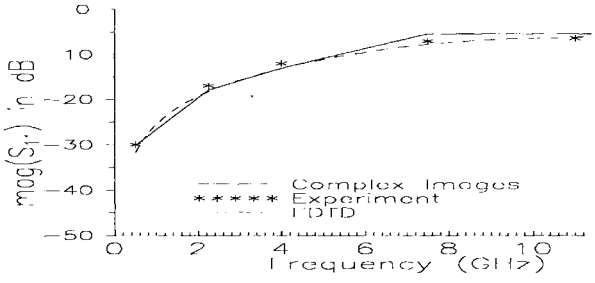

Fig. 6. Comparison between experimental results, complex image results, and FDTD results for $|S_{11}|$ of two aperture-coupled microstrips. ($W_u = W_L = 0.2028$ cm, $\varepsilon_u = \varepsilon_L = 2.94$, $h_u = h_L = 0.0762$ cm, $L = 0.96$ cm, $W = 0.068$ cm.)

been presented. This method uses a mixed electric–magnetic current integral equation formulation with moment-method and complex images. The results were compared with the FDTD method and experiments to demonstrate the accuracy of the proposed method.

Unlike the other methods presented in the literature to solve the transitions, the efficient application of the moment method (of discretizing only the strips and apertures) combined with the accurate

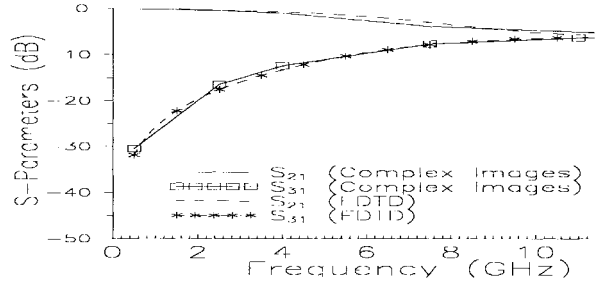

Fig. 7. Comparison between complex image results and FDTD results for $|S_{21}|$, $|S_{31}|$ of two aperture-coupled microstrips. (Dimensions are given in Fig. 6.)

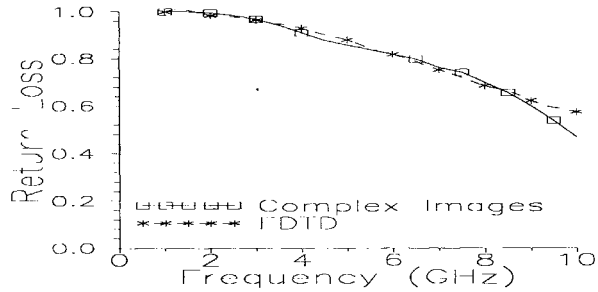

Fig. 8. The return loss versus frequency for MS–PWG transition ($W = h = 4$ mm, $\varepsilon_r = 2$, $L_s = 10$ mm, $a_a = 10$ mm, $b_a = 1$ mm, $D = 24$ mm.)

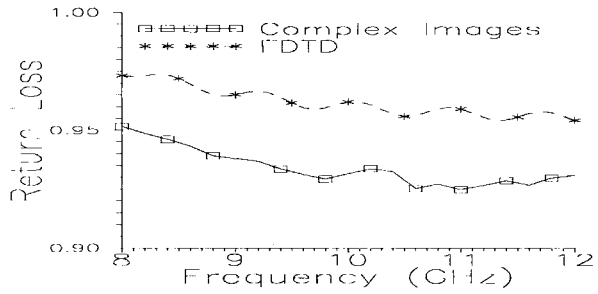

Fig. 9. The return loss versus frequency for MS–RW transition ($W = 2$ mm, $h = 0.8$ mm, $\varepsilon_r = 2.3$, $L_s = 4$ mm, $a_a = 5$ mm, $b_a = 1$ mm, $a = 23$ mm, $b = 10$ mm.)

and the rapidly convergent complex-image Green's functions, makes this method more suitable for use with optimization software to achieve optimum designs of the different transitions analyzed.

Appendix A: Complex Image Spatial Green's Functions ($G_{A_{xx}}$ and $G_{A_{zx}}$) in a Microstrip Substrate

The Green's functions ($G_{A_{xx}}$ and $G_{A_{zx}}$) in the space domain are derived using the complex image technique [4], [5]. The Green's functions given below are for the lower substrate where the ground plane is located at $z = 0$, the source is located at a general location (x, y, z) and the field is located at a general location (x', y', z'), where $-h \leq z,\ z' \leq 0$ (see Fig. 1). The corresponding Green's functions of the upper substrate can be easily obtained by replacing z with $-z$ and z' with $-z'$.

A. Green's Function for $G_{A_{xx}}$

Let k_ρ be the spectral variable, and k_{z_0}, k_{z_1} be related to k_ρ as follows:

$$k_{z_1}^2 + k_\rho^2 = k_0^2 \varepsilon_r, \qquad k_{z_0}^2 + k_\rho^2 = k_0^2. \tag{12}$$

Then the Green's function for $G_{A_{xx}}$ in the spectral domain is given by

$$\tilde{G}_{A_{xx}} = \frac{\mu_0}{j2k_{z_1}}\left\{e^{-jk_{z_1}|z-z'|} - e^{-jk_{z_1}|z+z'|} + \left[\sum_{\text{TEpoles}} \frac{j4\text{Res}_p k_{\rho p} k_{z_1}}{k_\rho^2 - k_{\rho p}^2} + G(k_p)\right] S_1(k_{z_1}, z, z')\right\} \quad (13)$$

where

$$S_1(k_{z_1}, z, z') = -e^{-jk_{z_1}(z-z'+2h)} - e^{-jk_{z_1}(-z+z'+2h)} + e^{-jk_{z_1}(z+z'+2h)} + e^{jk_{z_1}(z+z'-2h)} \quad (14)$$

$$G(k_\rho) = R_{\text{TE}} - \sum_{\text{TEpoles}} \frac{j4\text{Res}_p k_{\rho p} k_{z_1}}{k_\rho^2 - k_{\rho p}^2} \quad (15)$$

$$R_{\text{TE}} = \frac{r_{10}^{\text{TE}}}{D_{\text{TE}}}$$
$$r_{10}^{\text{TE}} = \frac{k_{z_1} - k_{z_0}}{k_{z_1} + k_{z_0}}$$
$$D_{\text{TE}} = 1 - r_{10}^{\text{TE}} e^{-j2k_{z_1}h}. \quad (16)$$

In (15), $k_{\rho p}$ and Res_p are, respectively, the TE pole and its residue given by

$$\text{Res}_p = \lim_{k_\rho \to k_{\rho p}} (k_p - k_{pp}) \frac{R_{\text{TE}}}{j2k_{z_1}}. \quad (17)$$

Using Prony's method [16], $G(k_\rho)$ can be approximated as follows:

$$G(k_\rho) = \sum_{i=1}^{N_{xx}} a_i^{xx} e^{-k_{z_1} b_i^{xx}} \quad (18)$$

where a_i^{xx} and b_i^{xx} are complex coefficients.

Performing the inverse Fourier transform of (13) and making use of the Sommerfeld identity and residue theorem [16], the spatial Green's function for $G_{A_{xx}}$ is given by

$$G_{A_{xx}}(\rho, z, z') = G_{A_{xx_0}} + G_{A_{xx,\text{sw}}} + G_{A_{xx,\text{CI}}} \quad (19)$$

where ρ is the radial distance between the source and field. The term $G_{A_{xx_0}}$ in (19) represents the contribution of the quasi-dynamic images, which are dominant in the near field, while the term $G_{A_{xx,\text{sw}}}$ represents the contribution of TE surface waves dominant in the far field, and the term $G_{A_{xx,\text{CI}}}$ represents the contribution of a set of images with complex amplitude and complex location, which are dominant in the intermediate field. These three contributions are given by

$$G_{A_{xx_0}} = \frac{\mu_0}{4\pi}\left\{\frac{e^{-jk_1 r_0}}{r_0} - \frac{e^{-jk_1 r_0'}}{r_0'}\right\} \quad (20)$$

$$G_{A_{xx,\text{sw}}} = \sum_{\text{TEpoles}} \frac{\mu_0}{4\pi}(-2\pi j)\text{Res}_p S_1(k_{z_1}, z, z') \quad (21)$$

$$G_{A_{xx,\text{CI}}} = \frac{\mu_0}{4\pi}\sum_{i=1}^{N_{xx}} a_i^{xx}\left[-\frac{e^{-jk_1 r_1}}{r_1} - \frac{e^{-jk_1 r_2}}{r_2} + \frac{e^{-jk_1 r_3}}{r_3} + \frac{e^{-jk_1 r_4}}{r_4}\right] \quad (22)$$

where

$$k_1 = k_0\sqrt{\varepsilon_r}$$
$$r_0 = \sqrt{\rho^2 + (z-z')^2}$$
$$r_0' = \sqrt{\rho^2 + (z+z')^2}$$
$$r_1 = \sqrt{\rho^2 + \left(z - z' + 2h - jb_i^{xx}\right)^2}$$
$$r_2 = \sqrt{\rho^2 + \left(-z + z' + 2h - jb_i^{xx}\right)^2}$$
$$r_3 = \sqrt{\rho^2 + \left(z + z' + 2h - jb_i^{xx}\right)^2}$$
$$r_4 = \sqrt{\rho^2 + \left(-z - z' + 2h - jb_i^{xx}\right)^2}. \quad (23)$$

B. Green's Function for $G_{A_{zx}}$

$$G_{A_{zx}} = \frac{\mu_0}{4\pi}\int_{-\infty}^{\infty} \frac{-jk_x}{(j2k_{z_1})jk_{z_1}} R_q S_2 H_0^{(2)}(k_\rho \rho) k_\rho \, dk_\rho \quad (24)$$

where $H_0^{(2)}$ is the Hankel function of the second kind of order zero, and

$$S_2(k_{z_1}) = 2e^{-jk_{z_1}(3h)} - 2e^{-jk_{z_1}(h)} \quad (25)$$

$$R_q = \frac{2(\varepsilon_r - 1)k_{z_1}^2}{(k_{z_0} + k_{z_1})(k_{z_1} + \varepsilon_r k_{z_0}) D_{\text{TE}} D_{\text{TM}}} \quad (26)$$

$$D_{\text{TM}} = 1 - r_{10}^{\text{TM}} e^{-j2k_{z_1}h}$$
$$r_{10}^{\text{TM}} = \frac{k_{z_1} - \varepsilon_r k z_0}{k_{z_1} + \varepsilon_r k_{z_0}} \quad (27)$$

and D_{TE} is given in (16).

Next, $-jk_x$ is replaced in (24) with $\frac{\partial}{\partial x}$, and the following Prony approximation are then performed:

$$\frac{R_q}{jk_{z_1}} S_2 = \sum_{i=1}^{N_{zx}} a_i^{zx} e^{-k_{z_1} b_i^{zx}} \quad (28)$$

where a_i^{zx} and b_i^{zx} are complex coefficients.

Substituting (28) in (24) and performing the integration using the Sommerfeld identity results in

$$G_{A_{zx}} = \frac{\mu_0}{4\pi}\sum_{i=1}^{N_{zx}} a_i^{zx} \frac{\partial}{\partial x}\frac{e^{-jk_1 r_i}}{r_i} \quad (29)$$

where

$$r_i = \sqrt{\rho^2 + \left(-jb_i^{zx}\right)^2}.$$

Appendix B:
Coupling Matrixes Between the Magnetic Current of the Aperture and the Electric Current on the Microstripline

Applying the Galerkin moment-method procedure and using the Gauss–Chebyshev integration rule to take care of the transverse current distribution functions τ_n^e and τ_n^m in (7) and (8) gives the following expression for the coupling matrix $Z_{me}^{(1)}$ of the lower sub-problem:

$$\left[Z_{me}^{(1)}\right] = \left[Z_{me}^{xx}\right] + \left[Z_{me}^{zx}\right] \quad (30)$$

$$V'(x, y, x', y') = \frac{-e^{-jk_1 r_i}\left\{\left[-k_1^2(x-x')^2 - jk_1 r_i - 1\right]r_i^2 + 3(x-x')^2(jk_1 r_i + 1)\right\}}{r_i^5} \quad (37)$$

where

$$Z^{xx}_{me}(m,n) = \frac{-1}{4\pi NM}\sum_{k=1}^{N}\sum_{L=1}^{M} I^{xx}_{m,n,k,L} \tag{31}$$

$$I^{xx}_{m,n,k,L} = \int_{l^e_{n,k}}\int_{l^m_{m,L}} V(x_L, y, x', y_k)\, dy dx' \tag{32}$$

where N and M represent the number of Gaussian quadrature nodes on the magnetic and electric segments, respectively. x_L and y_k are the Gaussian quadrature nodes on the aperture and microstrip, respectively, and $l^e_{n,k}$ and $l^m_{m,L}$ are the lengths of the electric and magnetic segments, respectively. Also

$$V(x,y,x',y') = 2h\frac{(-jk_1r_0 - 1)}{r_0^3}e^{-jk_1r_0} \tag{33}$$

where

$$r_0 = \sqrt{(x-x')^2 + (y-y')^2 + h^2}. \tag{34}$$

On the other hand

$$Z^{zx}_{me}(m,n) = \frac{-1}{4\pi NM}\sum_{i=1}^{N_{zx}} a_i^{zx}\sum_{k=1}^{N}\sum_{L=1}^{M} I^{zx}_{m,n,i,k,L} \tag{35}$$

where N_{zx} and a_i^{zx} are, respectively, the number and amplitude of the complex images of $G_{A_{zx}}$. Thus

$$I^{zx}_{m,n,i,k,L} = \int_{l^e_{i,n,k}}\int_{l^m_{m,L}} V'(x_L, y, x', y_k)\, dy\, dx' \tag{36}$$

$V'(x,y,x',y')$ is shown in (37) at the bottom of the previous page, and

$$r_i = \sqrt{\rho^2 + \left(-jb_i^{zx}\right)^2}. \tag{38}$$

ACKNOWLEDGMENT

The authors would like to thank the Communications research Centre in Ottawa, Ont., Canada for providing the experimental results of Fig. 6.

REFERENCES

[1] W. Grabherr and W. Menzel, "A new transition from microstrip line to rectangular waveguide," in *Proc. of 22nd EuMC*, Espoo, Finland, 1992, pp. 1170–1175.
[2] L. Hyvonen and A. Hujanen, "A compact MMIC-compatible microstrip to waveguide transition," in *IEEE MTT-S Dig.*, San Franciso, CA, June 1996, pp. 875–878.
[3] N. Herscovici and D. Pozar, "Full-wave analysis of aperture-coupled microstrip lines," *IEEE Trans. Microwave Theory Tech.*, vol. 39, pp. 1108–1114, July 1991.
[4] A. A. Omar and Y. L. Chow, "A solution of coplanar waveguide with air-bridges using complex images," *IEEE Trans. Microwave Theory Tech.*, vol. 40, pp. 2070–2077, Nov. 1992.
[5] Y. L. Chow, J. J. Yang, D. G. Fang, and G. E. Howard, "A closed form spatial Green's functions for thick microstrip substrates," *IEEE Trans. Microwave Theory Tech.*, vol. 39, pp. 588–593, Mar. 1991.
[6] K. Kunz and R. Luebbers, *The Finite Difference Time Domain Method for Electromagnetics*. Boca Raton, FL: CRC Press, 1993.
[7] J. Cheng, N. I. Dib, and P. B. Katehi, "Theoretical modeling of cavity-backed patch antennas using a hybrid technique," *IEEE Trans. Microwave Theory Tech.*, vol. 43, pp. 1003–1013, Sept. 1995.
[8] J. Yook, N. I. Dib, and P. B. Katehi, "Characterization of high frequency interconnects using finite difference time domain and finite element methods," *IEEE Trans. Microwave Theory Tech.*, vol. 42, pp. 1727–1736, Sept. 1994.
[9] R. S. Elliott, *Antenna Theory and Design*. Englewood Cliffs, NJ: Prentice-Hall, 1981.
[10] D. G. Fang, J. J. Yang, and K. Sha, "The exact images of a horizontal magnetic dipole above or within a microstrip substrate," in *Proc. Sino-Japanese Joint Meeting Optical Fiber Sci. and EM Theory*, Nanjing, China, 1987, pp. 693–698.
[11] R. E. Collin, *Field Theory of Guided Waves*. New York: McGraw-Hill, 1991, pp. 23–26.
[12] A. W. Glisson and D. R. Wilton, "Simple and efficient numerical methods for problems of electromagnetic radiation and scattering from surfaces," *IEEE Trans. Antennas Propagat.*, vol. AP-29, pp. 593–603, Sept. 1980.
[13] G. E. Howard, "Analysis of passive and active microwave integrated circuits by the field approach," M.A.Sc. thesis, Univ. Waterloo, Waterloo, Ont., Canada, 1988.
[14] R. F. Harrington, *Field Computation by Moment Methods*. Malabar, FL: R. E. Krieger, 1968, pp. 62–81.
[15] D. A. Huber, "A moment method analysis of stripline circuits through multi-pipe field modeling," M.A.Sc. thesis, Univ. Waterloo, Waterloo, Ont., Canada, 1991.
[16] R. W. Hamming, *Numerical Methods for Scientists and Engineers*. New York: Dover, 1973, pp. 620–622.
[17] A. A. Omar and Y. L. Chow, "Coplanar waveguide with top and bottom shields in place of air-bridges," *IEEE Trans. Microwave Theory Tech.*, vol. 41, pp. 1559–1563, Sept. 1993.

Effect of Conductor Backing on the Line-to-Line Coupling Between Parallel Coplanar Lines

Kwok-Keung M. Cheng

***Abstract*— A good estimate of the coupling effect between parallel coplanar waveguide (CPW) lines is important, especially for monolithic microwave integrated circuit (MMIC) applications where unnecessary crosstalk between conductors could be a serious problem. This paper shows how these coupling parameters may be analytically obtained in the presence of the back-face metallization. Closed-form formulas are developed for evaluating the quasi-TEM characteristic parameters based upon the conformal-mapping method (CMM). Very good agreement is observed between the values produced by these formulas and by a spectral-domain method (SDM).**

***Index Terms*—Coplanar waveguide, coupled lines.**

I. INTRODUCTION

Coplanar waveguide is often considered to have free space above and below the dielectric substrate. However, this configuration has been found unsuitable for monolithic microwave integrated circuits (MMIC's), where the substrate is typically thin and fragile. Practical realizations of coplanar waveguides (CPW's) usually have an additional ground plane beneath the substrate. The main advantages of this back-face metallization are principally to increase the mechanical strength as well as to improve heat dissipation. The standard CPW, plus this additional conducting ground plane, is often called conductor-backed CPW (CBCPW). Various approaches have been reported on the characterization of coplanar transmission lines such as the finite-difference method [1], the spectral-domain method

Manuscript received July 7, 1996; revised March 24, 1997.

The author is with the Department of Electronic Engineering, The Chinese University of Hong Kong, Shatin, Hong Kong.

Publisher Item Identifier S 0018-9480(97)04466-9.